



**HAL**  
open science

## Errors in PV power modelling due to the lack of spectral and angular details of solar irradiance inputs

N. Lindsay, Quentin Libois, Jordi Badosa, A. Migan-Dubois, Vincent Bourdin

### ► To cite this version:

N. Lindsay, Quentin Libois, Jordi Badosa, A. Migan-Dubois, Vincent Bourdin. Errors in PV power modelling due to the lack of spectral and angular details of solar irradiance inputs. *Solar Energy*, 2020, 197, pp.266-278. 10.1016/j.solener.2019.12.042 . hal-03080195

**HAL Id: hal-03080195**

**<https://hal.science/hal-03080195>**

Submitted on 17 Dec 2020

**HAL** is a multi-disciplinary open access archive for the deposit and dissemination of scientific research documents, whether they are published or not. The documents may come from teaching and research institutions in France or abroad, or from public or private research centers.

L'archive ouverte pluridisciplinaire **HAL**, est destinée au dépôt et à la diffusion de documents scientifiques de niveau recherche, publiés ou non, émanant des établissements d'enseignement et de recherche français ou étrangers, des laboratoires publics ou privés.

# Errors in PV power modelling due to the lack of spectral and angular details of solar irradiance inputs

N. Lindsay<sup>a</sup>, Q. Libois<sup>a,\*</sup>, J. Badosa<sup>b</sup>, A. Migan-Dubois<sup>c</sup>, V. Bourdin<sup>d</sup>

<sup>a</sup>CNRM, Université de Toulouse, Météo-France, CNRS; 42 Avenue Gaspard Coriolis, Toulouse, 31100, France

<sup>b</sup>LMD, IPSL, École Polytechnique, Université Paris-Saclay, ENS, PSL Research University, Sorbonne Université, CNRS ; Route de Saclay 91128 Palaiseau, France

<sup>c</sup>GeePs - Laboratoire Génie électrique et électronique de Paris, CNRS, SUPELEC, UPMC, University Paris-Sud 11; 11 rue Joliot-Curie, Plateau de Moulon, 91192 Gif-sur-Yvette Cedex, France

<sup>d</sup>LIMSI - Laboratoire d'Informatique pour la Mécanique et les Sciences de l'Ingénieur, CNRS; Rue John von Neumann, 91405 Orsay Cedex, France

---

## Abstract

Photovoltaic (PV) modules are sensitive to the spectral distribution of solar irradiance. Although numerical weather prediction (NWP) models compute irradiance in several spectral bands, only broadband quantities are provided in the standard outputs used for PV forecasts. This study investigates how this lack of information impacts PV power estimation. A physical PV model is first designed that accounts for the spectral distribution of irradiance and the spectral response of the panels. This model is evaluated using measurements performed at Site Instrumental de Recherche par Télédétection Atmosphérique (SIRTA), Palaiseau, France. The mean relative difference between simulated and measured PV power for a monocrystalline silicon module of 250 W nominal power is -0.9 %, and the mean bias is -2.0 W. This model is then used to investigate the impact of solar zenith angle and clouds on the performance of PV modules. PV performance can increase in cloudy conditions by 5 % through spectral filtering of near-infrared irradiance, and by 18 % when only the useful irradiance is considered to compute performance. This spectral effects is not captured by the PV model when only broadband irradiances are used. In such case errors up to 15 % are obtained in simulated PV power compared to using a state-of-the-art NWP model providing irradiance in 14 spectral bands. More generally, broadband global horizontal irradiance appears insufficient for accurate PV power modelling, highlighting the added value of spectrally-and-angularly-refined irradiances. This stresses that PV models should use more detailed irradiance inputs, which could be easily achieved by exploiting internal variables of NWP models.

**Keywords:** PV power, PV module performance, cloud–radiation interactions, spectral irradiance, numerical weather prediction

---

## 1 Introduction

Solar energy is characterised by large temporal fluctuations, in particular because it is sensitive to the presence and characteristics of clouds (Antonanzas et al., 2016). This variability is detrimental to the stability of the electricity grid, making the integration of solar energy at large scales challenging (e.g. Antonanzas et al., 2016). Correctly predicting the photovoltaic (PV) production of a solar farm at various time scales is thus a topical issue and has led to the development of a number of PV power forecast models which aim at computing PV power from weather forecasts (e.g. De Soto et al., 2006; King et al., 2004). These models can be either statistical or physical (Kostylev and Pavlovski, 2011; Diagne et al., 2013; Das et al., 2018), and this study focuses on physical PV models. In a physical model, all physical processes involved in the conversion of solar irradiance into electric power are successively modelled. This includes transposition (converting the solar irradiance on a horizontal surface into plane-of-array (POA) irradiance),

---

\*Corresponding author. Tel: +33 5 61 07 96 91  
Email address: quentin.libois@meteo.fr (Q. Libois)

## Nomenclature

$\alpha$	Spectral response correction factor	$R_{sh}$	Shunt resistance
$\beta$	Module inclination	$T_{mod}$	Module temperature
$\lambda$	Wavelength	$T_a$	Ambient temperature
$\lambda_{gap}$	Cutoff wavelength	$T_c$	Cell temperature
$\rho$	PV module performance	$T_g$	Transmittance of the global irradiance
$\rho^*$	PV module performance based on the useful POA irradiance	$U$	Wind speed
$\tau$	Cloud optical thickness	$V$	Load voltage
$SR_{ideal}$	Ideal spectral response	$V_{OC}$	Open-circuit voltage
$SR_{modelled}$	Modelled spectral response	$V_t$	Thermal voltage
$\theta_i$	Angle of incidence	APE	Average Photon Energy
$\theta_r$	Angle of refraction	ASTM	American Society for Testing and Materials
$a, b, \Delta T$	Empirical parameters	c	Speed of light
$C_{T, I_{SC}}$	Short-circuit current temperature coefficient	DC	Direct Current
$E_\lambda$	Photon energy	ECMWF	European Center Range Weather Forecast
$E_g$	Energy gap	FF	Fill Factor
$G$	Irradiance	GHI	Global Horizontal Irradiance
$g$	Asymmetry parameter	h	Planck constant
$G_{ASTM}$	Plane-Of-Array Irradiance for the ASTM spectrum	MM	Spectral mismatch factor
$G_{POA}$	Plane-Of-Array Irradiance	MRE	Mean Relative Error
$G_{ref}$	Reference spectrum	NOCT	Nominal Operating Cell Temperature
$G_{STC}$	STC reference spectrum	NWP	Numerical Weather Prediction
$G_c$	Cell-impacting irradiance	OL	Optical Losses
$I_0$	Reverse saturation current	POA	Plane-Of-Array
$I_{SC}$	Short-circuit current	PV	Photovoltaic
$I_D$	Photodiode current	SAA	Solar Azimuth Angle
$I_L$	Photogenerated current	SR	Spectral Response
$k$	Boltzmann constant	STC	Standard Test Conditions
$n_0$	Index of refraction of air	SW	Short-Wave
$n_1$	Index of refraction of glass	SZA	Solar Zenith Angle
$P$	Power	TOA	Top-Of-Atmosphere
$P_{MPP}$	Maximum power	UF	Useful Fraction
$q$	Elemental charge	USSA	US Standard Atmosphere
$R_s$	Series resistance		

11 optical losses, temperature variations of the PV cells and their electrical response to the cell-impacting irradiance. The  
 12 influence of temperature is significant, with typically a power reduction of 0.2% to 0.5% per degree difference from  
 13 25 °C for crystalline solar cells (Mittag et al., 2019), and has been widely studied. It is nowadays commonly accounted  
 14 for in PV models (e.g. King et al., 2004; Skoplaki et al., 2008). However, the PV cells constituting the module are also  
 15 sensitive to the spectral distribution of solar irradiance, as only sufficiently energetic photons generate current. This  
 16 has motivated studies (e.g. Marion, 2012; Stark and Theristis, 2015) on the impact of air mass, aerosol optical depth  
 17 and precipitable water – all affecting the spectral properties of radiation – on the performance of PV cells, hereafter  
 18 defined as the ratio of PV power to POA irradiance. For instance, direct and diffuse radiation in clear sky conditions

19 are known to result in different PV performances (Kirn and Topic, 2017). Likewise, the increase in PV performance  
20 under cloudy skies due to the shift of the spectrum towards the blue domain has been documented (e.g. Jardine et al.,  
21 2001; Nofuentes et al., 2014). These “spectral effects” have thus been observed for various technologies, locations,  
22 and seasons during observations campaigns (King et al., 1997; Jardine et al., 2001; Gottschalg et al., 2004; Ghitas,  
23 2012; Dirnberger et al., 2015), but they are not always properly accounted for in PV models.

24 Indeed, despite the recognized importance of the spectral effects (e.g. Nofuentes et al., 2017), PV models generally  
25 rely on variables provided by atmospheric models which only include broadband irradiance (i.e. integrated over the  
26 full short-wave (SW) domain). Consequently, the spectral distribution of the incident irradiance is unknown and the  
27 spectral effects are either neglected (e.g. Jerez et al., 2015) or accounted for through *ad hoc* correction factors (e.g.  
28 King et al., 2004). Spectral effects have thus been investigated via the average photon energy (APE) (Dirnberger et al.,  
29 2015), the useful fraction (UF) (Gottschalg et al., 2003), or the spectral mismatch factor (MM) (Nofuentes et al., 2014;  
30 Stark and Theristis, 2015; Dirnberger et al., 2015). However these quantities are not available from common weather  
31 products. Even more critically, atmospheric models sometimes only provide the global horizontal irradiance (GHI),  
32 in which case the partition between direct and diffuse is unspecified and also has to be parameterized (e.g. Gueymard  
33 and Ruiz-Arias, 2016).

34 Yet atmospheric models handle spectral irradiances as internal variables, which could be valuable for PV appli-  
35 cations. This spectral information is not usually output because atmospheric models resort to spectral bands only  
36 as an intermediate step to increase the accuracy of the broadband radiative budgets of the atmosphere and surface  
37 (e.g. RRTM, Mlawer et al., 1997). Similarly, the direct and diffuse components of radiation are internally computed,  
38 though they are rarely output. Extracting this spectral and angular information is practically straightforward as no  
39 extra computation is involved, and could be beneficial to PV power forecasts. This has for instance motivated the  
40 development of the Numerical Weather Prediction (NWP) model WRF-SOLAR (Jimenez et al., 2016).

41 Based on this observation, the primary objective of this paper is to investigate the benefit of using NWP solar  
42 irradiance outputs with detailed spectral and angular information compared to the standard broadband outputs. These  
43 benefits are assessed through a particular focus on cloud-radiation interactions and their impact on PV performance  
44 because clouds are mostly responsible for changes in spectral distribution. This implies comparing PV estimations  
45 obtained from standard outputs –broadband irradiance and sometimes only GHI– on the one hand, and from angularly  
46 and spectrally detailed outputs on the other hand. To this end, a dedicated physical PV model is developed that  
47 converts solar energy into electrical energy. It is similar to existing models in most respects, but includes a novel  
48 treatment of the spectral distribution of solar irradiance (Section 3). To validate this model, simulated PV power  
49 computed from GHI measurements are compared to PV power measurements made at the SIRTa, an atmospheric  
50 laboratory 20 km south of Paris, France (Haefelin et al., 2005). A theoretical sensitivity study is then performed by  
51 coupling the PV model with the state-of-the-art 14-band radiative transfer model ecRad (Hogan and Bozzo, 2018),  
52 operationally used at the European Center for Medium-Range Weather Forecast (ECMWF). To investigate the impact  
53 of the spectral and angular information of input irradiance in cloudy conditions, ecRad simulations are performed  
54 for ideal overcast conditions with homogeneous clouds and various solar zenith angles (SZA), and the corresponding  
55 surface irradiances fed into the PV code. To study the impact of the spectral resolution, the spectral outputs of ecRad  
56 are merged in order to virtually degrade the spectral information. The impact of angular information is investigated  
57 by comparing simulations where only GHI, or both the direct and diffuse irradiances, are provided. The results of  
58 these investigations are presented in Section 4. Finally, Section 5 highlights practical consequences of this academic  
59 study and provides more perspectives. Before that, however, Section 2 aims at providing some background knowledge  
60 about PV power and the effects of clouds on solar radiation.

## 61 2 Theoretical background

### 62 2.1 Photovoltaic effect

63 The photocurrent generated by a PV cell is highly dependent on the spectral characteristics of the impinging  
64 irradiance. The spectral sensitivity of PV cells is quantified by the spectral response (SR), which is the ratio between  
65 the photocurrent and the incident power at a given wavelength. Given that the energy of a photon  $E_\lambda$  is related to its  
66 wavelength  $\lambda$ , Planck constant  $h$  and the speed of light  $c$ :

$$E_\lambda = \frac{hc}{\lambda}, \quad (1)$$

67 the ideal SR reads :

$$68 \quad \text{SR}_{\text{ideal}}(\lambda) = \begin{cases} q \frac{\lambda}{hc}, & \text{if } \lambda < \lambda_{\text{gap}} \\ 0, & \text{otherwise} \end{cases}, \quad (2)$$

68 where  $q$  is the elemental charge. For a given incident power, the generated current increases linearly with wavelength  
 69 up to the cutoff wavelength  $\lambda_{\text{gap}}$ . Above  $\lambda_{\text{gap}}$ , it drops to zero as the photons are no longer energetic enough to excite  
 70 electrons. The useful irradiance is hereafter defined as the integrated irradiance up to  $\lambda_{\text{gap}}$ .

## 71 2.2 Impact of clouds on solar radiation

72 Clouds primarily alter PV power by reducing transmitted irradiance at the surface. However, for a given POA  
 73 irradiance, PV power (or equivalently PV performance) also depends on the spectral and angular distributions of  
 74 incoming irradiance, which is also altered by clouds. This paper investigates the importance of spectral and angular  
 75 details of irradiance inputs for PV power modelling through this specific impact of clouds on the performance of PV  
 76 modules. The transmittance of a homogeneous cloud mostly depends on its optical thickness, single scattering albedo  
 77 and asymmetry parameter (e.g. Kokhanovsky, 2004). The single scattering albedo mostly depends on the absorption  
 78 coefficient of liquid water, shown in Fig. 1. It highlights that water absorbs much more radiation in the near-infrared  
 79 (NIR) than in the visible. This spectral signature is also found in cloud transmittance (Fig. 1), with differences close  
 80 to 10% across the useful spectral range for a cloud with optical thickness 5. This demonstrates that clouds act as  
 81 spectral filters. As they mainly absorb those photons that cannot be absorbed by solar cells (e.g. wavelengths above  
 82  $\lambda_{\text{gap}} \sim 1100$  nm for c-Si technology), clouds tend to increase PV performance relative to clear sky. In addition, the  
 83 spectral distribution of irradiance for  $\lambda \leq \lambda_{\text{gap}}$  will be significantly different under clear and cloudy skies.

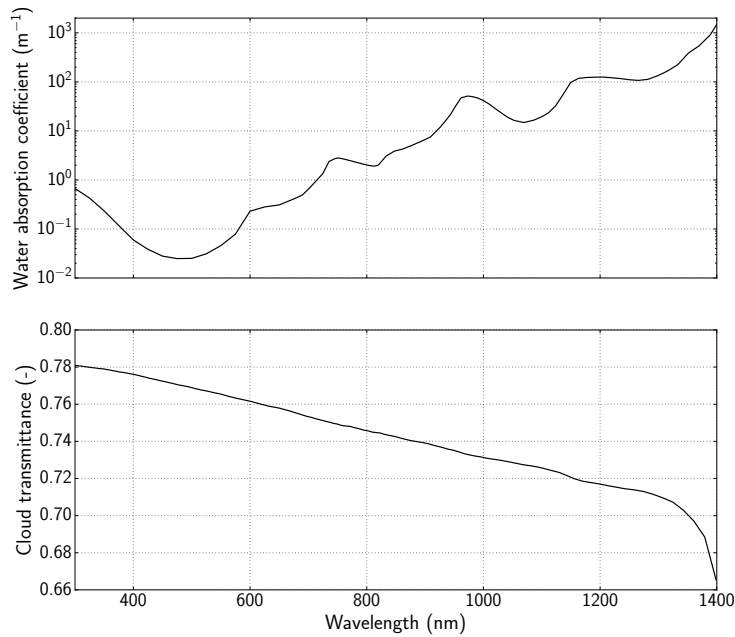


Figure 1: (top) Absorption coefficient of liquid water computed from the refractive index of Hale and Querry (1973). This database was also used to compute the cloud optical properties in ecRad (Section 3). (bottom) Spectral transmittance of a cumulus cloud of optical thickness 5 computed with ARTDECO (Section 3).

84 Figure 2 shows the atmospheric transmittance and the partition between direct and diffuse irradiance as a function  
 85 of cloud optical thickness in a clean (i.e. without aerosols) atmosphere. It shows that the partition is very sensitive to  
 86 cloud characteristics, especially for optical thicknesses below 20. The distinction between direct and diffuse radiation  
 87 is critical not only to characterise the angular properties of irradiance, but also its spectral distribution. Indeed, while

88 diffuse radiation in clean and clear conditions mainly comes from Rayleigh scattering, resulting in a distribution  
 89 peaking in the blue domain, direct radiation is more evenly distributed over the spectrum (Fig. 3). As a consequence,  
 90 direct radiation is generally slightly more efficient than diffuse radiation for PV power.

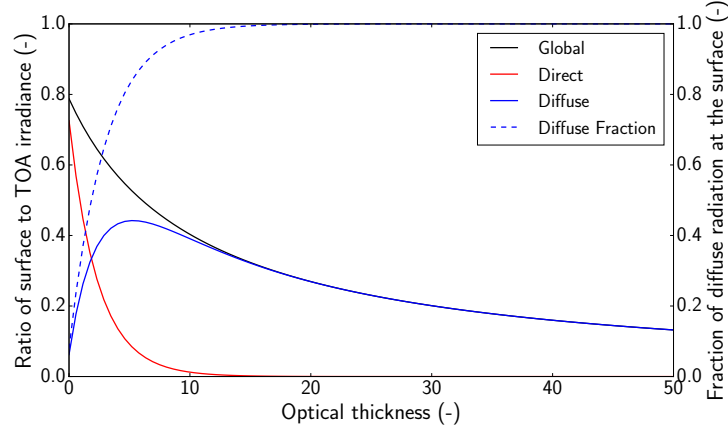


Figure 2: Atmospheric transmittance (computed as the ratio of surface to Top-Of-Atmosphere (TOA) irradiance), partition into direct and diffuse components (solid lines) and fraction of diffuse radiation at the surface (dashed line) as a function of cloud optical thickness, simulated with ecRad (Section 3) using the US Standard Atmosphere 1976 without aerosols. SZA equals  $48^\circ$  and the sky is overcast by a homogeneous cloud. Note that ecRad uses the  $\delta$ -Eddington approximation (Joseph et al., 1976) approximation, so that direct radiation includes some radiation that has been forward scattered.

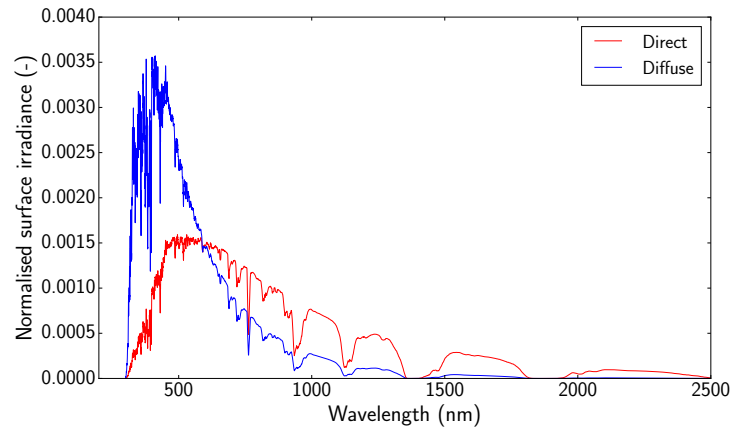


Figure 3: Clear-sky direct and diffuse solar irradiances, simulated with ARTDECO. The US Standard Atmosphere 1976 without aerosols is used, and SZA =  $48.2^\circ$ . The surface albedo corresponds to vegetation. Both spectra were normalised to have unit integrals.

### 91 3 Data and Methods

#### 92 3.1 In situ observations dataset

93 In this study, an exhaustive dataset including atmospheric and PV measurements from SIRTa (Palaiseau, France)  
 94 over the period January 2015 – June 2017 is used (Badosa et al., 2015) to evaluate the developed PV model. The focus  
 95 is on a single PV monocrystalline silicon (c-Si) module (France Watts, 250 W nominal power, South-facing with an  
 96 inclination of  $27^\circ$ ), whose operating conditions are monitored (module temperature  $T_{\text{mod}}$ , and I-V curve character-  
 97 isation from which the PV maximum power  $P_{\text{MPP}}$ , the fill factor FF and the open-circuit voltage  $V_{\text{OC}}$  are derived).  
 98 Although other technologies with lower  $\lambda_{\text{gap}}$  are known to be more sensitive to spectral effects, c-Si technology was

99 chosen for this study because it is widely used and offers good PV performance. GHI and the diffuse horizontal irradiance are measured thanks to a CMP22 Kipp & Zonen Pyranometer and the POA irradiance with a SR01 Hukseflux  
100 pyranometer. Wind speed and air temperature are also available. All data are 10-minute averaged variables in order to  
101 account for the 700 m distance between some of the instruments which could induce inconsistencies at shorter time  
102 scales, and to overcome any issues due to differing sampling frequencies between instruments.  
103

### 104 3.2 Radiative transfer codes

105 Two radiation codes are used in this study. ARTDECO<sup>1</sup> is used to compute a set of reference clear-sky spectra  
106 at high spectral resolution. These spectra are used in the PV model. ecRad is used for the sensitivity study to clouds  
107 because it mimics irradiance outputs of NWP models.

108 ARTDECO is a versatile and user-friendly radiative transfer model recently developed at Laboratoire d'Optique  
109 Atmosphérique (Lille, France) by the French atmospheric radiative transfer community (e.g. Frouin et al., 2018).  
110 Here it is run at  $10\text{ cm}^{-1}$  resolution with a correlated- $k$  distribution and uses the DISORT model (Stamnes et al.,  
111 1988) to solve the radiative transfer equation. It is thus similar to libRadtran (Mayer and Kylling, 2005) in terms of  
112 capabilities and performances. The reference spectra are computed for atmospheric conditions as close as possible  
113 to the standard conditions used to compute the ASTM (American Society for Testing and Materials) solar spectrum  
114 G173-03. For this reason, the United States Standard Atmosphere (USSA) 1976 is used. Because the *rural* aerosols  
115 profile commonly used to compute the ASTM spectrum is not available in ARTDECO, sulfate aerosols are included  
116 in the profile instead. Adding sulfate aerosols at 50 % relative humidity from the OPAC database (Hess et al., 1998)  
117 with an optical depth of 0.06 at 550 nm allowed to reproduce the standard  $1000\text{ W m}^{-2}$  of the ASTM spectrum once  
118 projected on the module. This aerosol load is thus used to compute the reference spectra. The surface spectral albedo  
119 is set to that of vegetation. The direct and diffuse spectra are computed for a variety of SZAs. In Section 3.3.3, these  
120 spectra are used to refine the spectral resolution of irradiance outputs. The high spectral resolution allows to account  
121 for the detailed spectral distribution of incident solar radiation, especially around  $\lambda_{\text{gap}}$ . Note that the reference spectra  
122 could have alternatively been obtained with the SMARTS model (Myers and Gueymard, 2004) or libRadtran.

123 ecRad is the radiation code implemented in the Integrated Forecast System (IFS) of ECMWF. Here its standalone  
124 version is used<sup>2</sup>, meaning that it is fully external to the IFS code and can be used as any other radiative transfer code.  
125 ecRad is a two-stream model based on correlated- $k$  distributions. Given a vertical description of the atmosphere, it  
126 computes SW radiative fluxes in the spectral bands corresponding to those of the Rapid Radiative Transfer Model  
127 (RRTM, Mlawer et al., 1997; Morcrette et al., 2008) as detailed in Table 1. RRTM is extensively used in the weather  
128 and climate community (e.g. Oreopoulos et al., 2012). All ecRad simulations are performed with the USSA 1976  
129 (Myers et al., 2002) as a background atmosphere. ecRad has the capability to handle aerosols. The latter have to  
130 be described in terms of their type, and vertical distribution of mass mixing ratio. Within the IFS, ecRad compu-  
131 tations include the aerosols provided by the host model, which vary in space and time. However in the sensitivity  
132 study the simulations are performed without aerosols because 1) it seeks at isolating the physical processes related to  
133 clouds hence prevents any competition between cloud and aerosols radiative effects; 2) any choice of aerosol vertical  
134 distribution and type would have been arbitrary and; 3) the sensitivity study is intentionally an academic exercise.  
135 The broadband surface albedo is set to 0.2, a typical broadband value for grassland (e.g. Lohou and Patton, 2014).  
136 To study the influence of clouds, a 1-km-thick homogeneous cloud is added to the USSA atmosphere. It is located  
137 between 2 and 3 km with droplets effective radius of  $10\text{ }\mu\text{m}$ . Its optical thickness, computed after the parameterization  
138 of Edwards and Slingo (1996), is varied by varying its liquid water mixing ratio. Although this ideal cloud geometry  
139 does not encompass the variety and complexity of natural cloud structures (e.g. multi-layer clouds, broken clouds,  
140 thin cirrus clouds), it is consistent with the crude representation of clouds in NWP and climate models, and is often  
141 used in theoretical radiative transfer studies (e.g. Nielsen et al., 2014). It will provide a first quantitative assessment  
142 of the effect of clouds on PV performance in the framework of NWP models. However an exhaustive assessment of  
143 cloud effects on PV power is beyond the scope of this study and would require 3D radiative transfer computations  
144 performed on realistic cloud fields, which is far from the capabilities of operational NWP models.

<sup>1</sup>freely available from <http://www.icare.univ-lille1.fr/projects/artdeco>

<sup>2</sup>freely available for research from <https://confluence.ecmwf.int/display/ECRAD/ECMWF+Radiation+Scheme+Home>

Table 1: Wavenumber and wavelength limits of the 14 SW bands in ecRad.

Wavenumber $\text{cm}^{-1}$		Wavelength $\mu\text{m}$	
Minimum	Maximum	Minimum	Maximum
820	2600	3.84	12.2
2600	3250	3.07	3.84
3250	4000	2.50	3.07
4000	4650	2.15	2.50
4650	5150	1.94	2.15
5150	6450	1.55	1.94
6450	7700	1.29	1.55
7700	8050	1.24	1.29
8050	12850	0.778	1.24
12850	16000	0.625	0.778
16000	22650	0.442	0.625
22650	29000	0.345	0.442
29000	38000	0.263	0.345
38000	50000	0.200	0.263

### 145 3.3 The photovoltaic model

#### 146 3.3.1 Overall approach

147 The developed PV model relies on the “one-diode model” (Fig. 4) as in Lorenzo (2003), assuming a constant  
 148 series resistance  $R_s$  and an infinite shunt resistance  $R_{sh}$  (i.e. its effects are neglected). In the following, both power  
 149 and current are defined per unit area to be consistent with the irradiance provided per unit area.

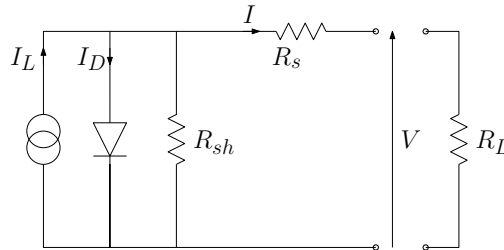


Figure 4: Equivalent electrical circuit of a solar cell, with  $I_D$  the photodiode current,  $I_L$  the photogenerated current, and  $R_L$  and  $V$  the load resistance and voltage.

150 The fill factor FF, the short-circuit current  $I_{SC}$  and the open-circuit voltage  $V_{OC}$  are independently computed to  
 151 obtain the maximum power  $P_{MPP}$ . In the rest of this study, it is assumed that the operating point is the maximum power  
 152 point (MPP). Note that this work only models the direct current (DC) side of PV power. To have a complete estimation  
 153 for a real PV system, further considerations would be necessary, like the eventual mismatch between modules in the  
 154 same string, possible losses from the inverter MPP tracker strategies and the inverter efficiency that typically depends  
 155 on the input DC power, among other factors.

156 As  $R_{sh} = \infty$ ,  $I_{SC}$  equals the photogenerated current  $I_L$ . Hence it is directly related to the amount of solar energy  
 157 converted into electric current, which depends on the spectral irradiance impinging on the module  $G(\lambda)$ , the spectral  
 158 response of the material  $SR(\lambda)$  and the cell temperature  $T_c$ :

$$I_{SC} = \left[ \int_{\lambda} SR(\lambda)G(\lambda)d\lambda \right] \cdot (1 + C_{T,I_{SC}} \cdot (T_c - T_{c,STC})) \quad (3)$$



159 with  $C_{T,I_{SC}}$  the short-circuit current temperature coefficient provided by the manufacturer accounting linearly for tem-  
 160 perature effects <sup>3</sup>. Such a formulation accounts for the spectral and temperature effects but requires a fine spectral  
 161 resolution irradiance at the cell-level, as well as an accurate estimation of the spectral response and the cell temper-  
 162 ature. The other parameters ( $C_{T,I_{SC}}, T_{c,STC}$ ) are provided by the manufacturer. With these notations, the APE (e.g.  
 163 Norton et al., 2015) is defined as:

$$APE(\lambda) = \frac{\int_{\lambda} G(\lambda) d\lambda}{\int_{\lambda} SR_{ideal}(\lambda) G(\lambda) d\lambda}. \quad (4)$$

164  $V_{OC}$  is modelled as Da Rosa (2005); Messenger and Abtahi (2017):

$$V_{OC} = V_t \ln\left(\frac{I_{SC}}{I_0}\right). \quad (5)$$

165 It mainly depends on  $T_c$  through the thermal voltage  $V_t = kT_c/q$  term (with  $k$  the Boltzmann constant) and  $I_0$  the  
 166 reverse saturation current which is highly sensitive to temperature and computed following Singh and Ravindra (2012):  
 167

$$I_0(T_c) = CT_c^3 \cdot \exp\left(-\frac{E_g}{kT_c}\right). \quad (6)$$

168 The constant  $C$  is deduced from the manufacturer datasheet <sup>4</sup>. The temperature dependency of the energy gap  $E_g$  is  
 169 neglected, according to Singh and Ravindra (2012).

170 FF is computed following eq. (7) of Green (1982) and depends on  $I_{SC}$ ,  $V_{OC}$ ,  $V_t$  and  $R_s$ .  $R_s$  is assumed constant,  
 171 and is computed by inverting the formulation of Green (1982) based on the STC characteristics.

172 To summarize, the PV model requires the cell temperature  $T_c$ , the spectral response  $SR(\lambda)$  and the cell impacting  
 173 spectral irradiance  $G(\lambda)$ . The following details how these variables are computed from variables commonly output  
 174 by atmospheric models, namely direct and diffuse horizontal incident irradiances, air temperature and wind speed.  
 175 Figure 5 illustrates the architecture of the PV model.

### 176 3.3.2 Cell temperature and spectral response

177 a) *Cell temperature.*  $T_c$  is modelled after King et al. (2004). First, the module temperature  $T_{mod}$  is computed from  
 178 the air temperature  $T_a$ , the POA irradiance  $G_{POA}$  and  $U_{10m}$  the wind speed at 10 m (King et al., 2004):

$$T_{mod} = G_{POA} \exp(a + b \times U_{10m}) + T_a, \quad (7)$$

179 where  $a = -3.23$  and  $b = -0.13 \text{ s m}^{-1}$  were chosen from the parameters provided in King et al. (2004) because they  
 180 resulted in the best match with measured module temperatures.  $T_c$  is then derived from  $T_{mod}$ :

$$T_c = T_{mod} + \frac{G_{POA}}{G_{ref}} \times \Delta T \quad (8)$$

181 where  $\Delta T = 13\text{K}$  for  $G_{ref} = 1000 \text{ W m}^{-2}$  is also taken from King et al. (2004).

<sup>3</sup>The STC subscript refers to the Standard Test Conditions (Sun-facing module with an inclination of  $\beta_{STC} = 37^\circ$ , incident irradiance of  $1000 \text{ W m}^{-2}$  with the solar spectrum for an air mass of 1.5, cell temperature  $T_{c,STC} = 25^\circ\text{C}$ )

<sup>4</sup>One can easily deduce from Eq. 5 and Eq. 6 that  $C = I_{SC,STC} (T_{c,STC})^{-3} \exp\left(\frac{E_g}{q} - \frac{V_{OC,STC}}{V_t(T_{c,STC})}\right)$

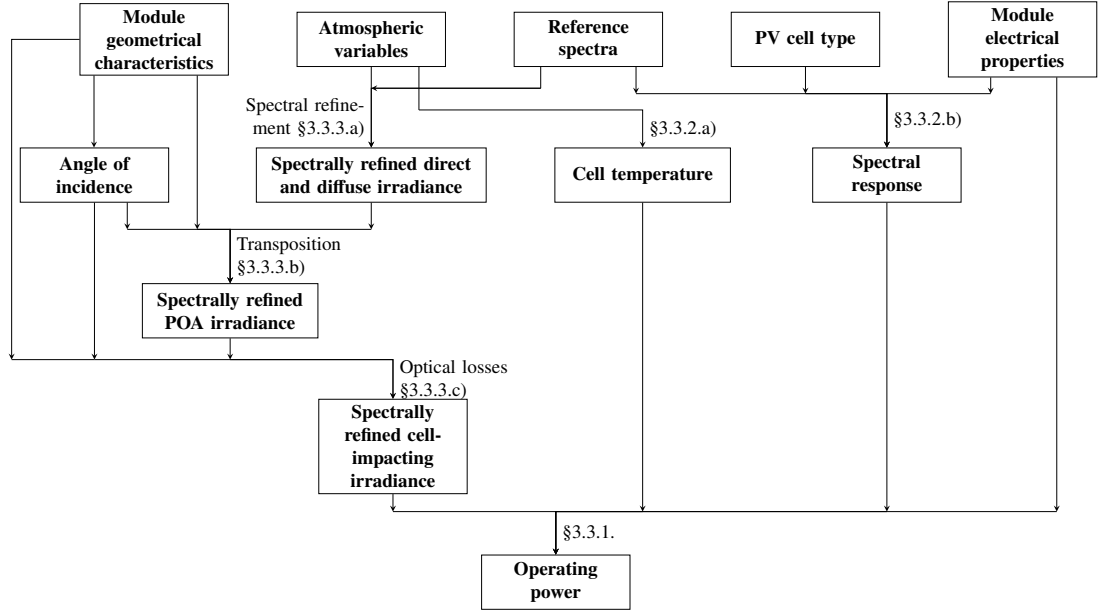


Figure 5: Simplified workflow of the PV model.

182 *b) Spectral response.* Contrary to the ideal SR introduced in Section 2.1, the actual SR is specific to each individual  
 183 module because a reduced response can be caused by module-specific factors like surface recombination, non-optimal  
 184 absorption or ageing. Unless the SR is provided by the user, a systematic approach based on the ideal formulation is  
 185 used. It consists in scaling the ideal spectral response by a factor  $\alpha$ :

$$\text{SR}_{\text{modelled}}(\lambda) = \alpha \times \text{SR}_{\text{ideal}}(\lambda). \quad (9)$$

186  $\alpha$  is set such that the current is correctly computed in STC. It is computed as:

$$\alpha = \frac{I_{\text{SC,STC}}}{\int_{\lambda} \text{SR}_{\text{ideal}}(\lambda) G_{c,\text{ASTM}}(\lambda) d\lambda}, \quad (10)$$

187 with  $G_{c,\text{ASTM}}$  the cell-impacting irradiance resulting from an incoming ASTM reference spectrum in the POA, ac-  
 188 counting for optical losses. Here  $\alpha = 0.77$ . The constant  $\alpha$  remains however dependent on the module considered,  
 189 as the ideal spectral response relies on  $\lambda_{\text{gap}}$ , which is technology-specific. Note that taking a more realistic spectral  
 190 response may alter the following results, as discussed in Section 4.2.

### 191 3.3.3 Cell impacting spectral irradiance

192 Whereas the previous components of the PV code were essentially built from the literature, the novelty of the  
 193 code is the subsequent treatment of spectral irradiance, which allows to get  $G(\lambda)$  at high spectral resolution whatever  
 194 the resolution of the irradiance input. It is assumed that the direct and diffuse horizontal irradiances are provided in  
 195 a limited number of spectral bands. If only the GHI is provided, a preliminary step should be used to decompose  
 196 GHI into direct and diffuse irradiance. The cell impacting spectral irradiance is modelled by first computing the  
 197 POA irradiance from the direct and diffuse components (transposition step detailed below), then by applying optical  
 198 losses which account for reflection at the surface of the module. The cell impacting irradiance, later convolved by the  
 199 SR, should have a spectral resolution fine enough to account for the spectral dependence of the SR and in particular  
 200 its sharp discontinuity around  $\lambda_{\text{gap}}$ . To this end, the low resolution direct and diffuse horizontal irradiances are first  
 201 manipulated to reach the resolution of the reference ARTDECO spectra. The procedure is detailed below.

202 *a) Refining the spectral resolution.* The refinement of spectral resolution aims at detailing the relative distribution  
 203 of energy within each spectral band of the input irradiances. This is achieved by applying the resolution and shape  
 204 of a reference spectrum  $G_{\text{ref}}$  to the narrow-band spectrum whilst conserving the total amount of energy within each  
 205 band. The fine resolution irradiance for  $\lambda \in [\lambda_k; \lambda_{k+1}]$  (where  $\lambda_k$  and  $\lambda_{k+1}$  are the lower and upper boundaries of band  
 206  $k$ ) is computed as follows:

$$G(\lambda) = G_k \frac{G_{\text{ref}}(\lambda)}{\int_{\lambda_k}^{\lambda_{k+1}} G_{\text{ref}}(\lambda) d\lambda}, \quad (11)$$

207 where  $G_k$  is the irradiance in band  $k$ . This method leads to discontinuities at each band limit but allows to better  
 208 account for the actual distribution within a band. Note that commonly used quantities such as APE, MM and UF can  
 209 all be computed from  $G(\lambda)$ .

210 The choice of the reference spectrum is key to accurately inform about the spectral distribution of irradiance. Given  
 211 that direct and diffuse irradiances have very distinct spectral distributions, both components are spectrally refined  
 212 separately using direct and diffuse reference spectra. The spectral distribution also depends on SZA and atmospheric  
 213 conditions (Liou, 2002). To account for this, a collection of clear-sky reference spectra is considered, with SZA  
 214 ranging from  $5^\circ$  to  $85^\circ$  by steps of  $5^\circ$ . All reference spectra are computed with the same atmospheric characteristics  
 215 (water vapour, ozone, aerosols). Extending the set of reference spectra to other variables would substantially increase  
 216 the complexity of the model. Furthermore, the exact atmospheric conditions are already properly accounted for in  
 217 the total energy per band provided by the irradiance inputs, which is conserved when refining the resolution. Only  
 218 changes in spectral shape within a band might be missed with this limited set of reference spectra, but this is secondary  
 219 with regards to the general shape of a solar spectrum. In other terms, limiting the reference spectra to only various  
 220 SZAs enables us to keep the model simple whilst explaining most features of the spectral distribution.

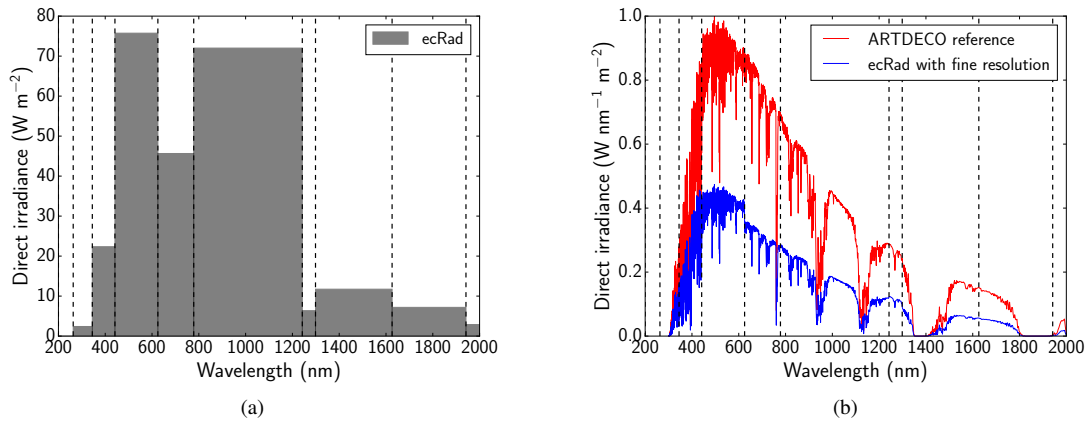


Figure 6: Illustration of the spectral refinement step used in the PV model. (a) Low-resolution direct irradiance computed by ecRad for a thin cloud with optical thickness 2.3. (b) Corresponding ARTDECO clear-sky direct irradiance at the same SZA, and spectrally refined ecRad irradiance using the reference spectrum. The dotted lines indicate ecRad bands.

221 Figure 6 illustrates the steps required for refining the spectral resolution of direct surface irradiance obtained from  
 222 ecRad in the case of an optically thin cloud ( $\tau = 2.3$ ). The reference spectrum is computed by interpolation of  
 223 the direct ARTDECO spectra for the given SZA (Fig. 6b). The initial irradiance (Fig. 6a) is then spectrally refined  
 224 following Eq. 11 which leads to a spectrum of the same resolution as the reference spectrum (Fig. 6b).

225 *b) Transposition.* Transposition of the direct component on the POA simply depends on SZA, SAA (Solar Azimuth  
 226 Angle), and the module inclination and azimuth (Duffie and Beckman, 2013). For the diffuse component, a hypothesis  
 227 on the angular distribution over the sky dome is required to account for the equivalent angle-of-incidence on the  
 228 module. A variety of transposition models are available in the literature. Here, it is chosen based on a thorough

229 comparison of broadband POA irradiances measured at the SIRTAs on the one hand, and computed from direct and  
 230 diffuse broadband horizontal irradiances on the other hand. Practically, it follows the approach from Badescu (2002)  
 231 for  $\text{SZA} < 70^\circ$  and Perez et al. (1990) otherwise. The ground-reflected component follows the approach from Badescu  
 232 (2002) except for  $\text{SZA} > 70^\circ$  where the 2D isotropic model (e.g. Duffie and Beckman, 2013) is applied. Although  
 233 these choices were constrained by very specific observations, they are sufficiently physically relevant to meet our  
 234 objectives. Note also that these parameterisations were initially developed for broadband quantities but are extended  
 235 here to spectrally-refined irradiances.

236 *c) Optical losses.* Optical losses result from reflection at the panel surface. Although they are wavelength-dependent,  
 237 Sjerps-Koomen et al. (1996) show that this dependence can be neglected. They also conclude that optical losses mostly  
 238 result from the air-glass interface. For this reason, the optical losses OL applied here correspond to the proportion of  
 239 incident radiation that is reflected at the air-glass interface (Sjerps-Koomen et al., 1996):

$$\text{OL} = \frac{1}{2} \left( \frac{\sin^2(\theta_i - \theta_r)}{\sin^2(\theta_i + \theta_r)} + \frac{\tan^2(\theta_i - \theta_r)}{\tan^2(\theta_i + \theta_r)} \right), \quad (12)$$

240 with  $\theta_i$  and  $\theta_r$  the angles of incidence and refraction at the air-glass interface.  $\theta_i$  is computed from the SZA, SAA and  
 241 module orientation and  $\theta_r$  is computed after Snell's law :

$$\theta_r = \arcsin \left( \frac{n_0}{n_1} \sin(\theta_i) \right), \quad (13)$$

242 with  $n_0 = 1$  and  $n_1 = 1.526$  the refractive indexes of air and glass (De Soto et al., 2006). Note that this approach  
 243 does not consider any antireflective coating. Adding such a layer would imply adding module specific parameters not  
 244 informed by the manufacturer datasheet. Furthermore, this simple model already corrected most errors in PV power  
 245 at low SZA when validating against measurements at SIRTAs. Given the difference in effective angle-of-incidence for  
 246 direct, diffuse and reflected contributions to POA irradiance, the optical losses are computed independently for all three  
 247 components. The effective incident angle for diffuse and reflected components are computed following Brandemuehl  
 248 and Beckman (1980).

### 249 3.4 Code validation

250 The PV model has been validated against SIRTAs measurements spanning January 2015 – June 2017. The mea-  
 251 sured broadband global and diffuse irradiances, wind speed and air temperature are used as inputs to the PV model.  
 252 The spectral surface albedo is that of vegetation to be consistent with SIRTAs environment. Over the whole period,  
 253 when  $\text{SZA} < 80^\circ$ , the simulated PV power for the 250 W panel has a mean relative error (MRE<sup>5</sup>) of -0.9 %, a mean  
 254 bias of -2.0 W and a root mean squared error of 13.2 W compared to observations. The MRE is chosen instead of the  
 255 mean error to stress that the model behaves well even at grazing solar angles.

256 The measured PV power has been regressed against the simulated POA irradiance (correlation coefficient  $r =$   
 257 0.970), the simulated POA irradiance corrected for temperature<sup>6</sup> ( $r = 0.972$ ) and the simulated PV power ( $r = 0.977$ ).  
 258 Although the differences are small, the correlation coefficients suggest that simulated PV power is more informative  
 259 than simulated POA. They also suggest that using a detailed PV model to treat the spectral effects is as crucial as  
 260 accounting properly for the temperature effect on  $P_{\text{MPP}}$ . This added value would certainly be more significant if the  
 261 inputs to the PV model were not broadband, but instead featured several spectral bands to better constrain the spectral  
 262 distribution of incident irradiance.

263 The PV model performs well under clear skies with no systematic bias. Figure 7 shows the measured and simulated  
 264 PV power over a period of seven consecutive cloudy days. In overcast conditions the PV model tends to underestimate  
 265 the power. This probably stems from the fact that reference spectra are clear-sky, meaning that the actual useful  
 266 fraction of irradiance is underestimated. The choice of the transposition model for diffuse radiation and the complex  
 267 irradiance fields due to scattered clouds can also contribute to the observed differences.

---

<sup>5</sup>  $\text{MRE} = \frac{1}{N} \sum_{i=1}^N \frac{P_{\text{sim}}^i - P_{\text{MPP}}^i}{P_{\text{MPP}}^i}$ .

<sup>6</sup> that is POA irradiance multiplied by  $(1 - C_{T,P_{\text{MPP}}}(T - T_{c,\text{STC}}))$  to include the effect of temperature on  $P_{\text{MPP}}$  provided by the manufacturer.

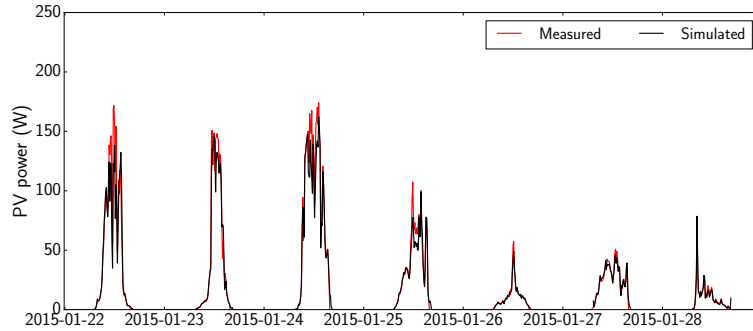


Figure 7: Measured and simulated PV power at SIRTa over a period of seven cloudy days.

268 Although informative, this evaluation does not fully bring out the potential and novelty of this code, as the inputs  
 269 are broadband. Furthermore, the errors can be due to the distance between the irradiance measurements fed into the  
 270 PV code and the effective position of the PV modules ( $\sim 700$  m). Also, the model has only been validated for one  
 271 site, and would deserve to be validated at other locations, in particular with other cloud regimes. Last, the PV model  
 272 does not require any measurements of the POA irradiance or PV power and fully relies on the datasheet provided by  
 273 the manufacturer, which has not been rigorously verified. As a consequence, any deviation from the specifications is  
 274 detrimental to the PV model. The focus of this paper is not on the absolute performance of this model, though. The  
 275 model was more designed as a physically comprehensive tool to study the influence of spectral and angular details of  
 276 surface solar irradiance on PV performance through the impact of clouds.

### 277 3.5 Sensitivity of simulated PV power to atmospheric inputs

278 In the rest of this study, a c-Si module is considered with an inclination of  $27^\circ$  (identical to the one used for the  
 279 code validation) to mimic the setup at SIRTa. The influence of clouds on PV performance estimation is studied by  
 280 providing ecRad spectra to the PV model. ecRad simulations are performed for various SZA and optical thicknesses  
 281 of the 1 km-thick cloud. The 14-band direct and diffuse horizontal irradiances outputs are input to the PV model  
 282 to simulate the PV power. The cell temperature is set constant to STC temperature, such that irradiance is the only  
 283 variable affecting PV power. In the following, two performance definitions are discussed: the standard performance  
 284  $\rho$  defined as the ratio of PV power to broadband POA irradiance and the in-band performance  $\rho^*$ . The latter only  
 285 considers the useful POA irradiance (i.e. up to  $\lambda_{\text{gap}}$ ).

286 The impact of spectral and angular details on the modelled PV power is studied based on the same ecRad inputs.  
 287 The 14-band direct and diffuse horizontal irradiances (Fig. 8a) are postprocessed to constitute three declined levels  
 288 of information: they are first integrated over every 2 consecutive bands resulting in a 7-band input (Fig. 8b) and then  
 289 over all bands leading to a 1-band input (Fig. 8c) for the PV model. A further degradation is considered by summing  
 290 the direct and diffuse components of the 1-band irradiance (Fig. 8d). In this case, the decomposition between direct  
 291 and diffuse irradiance follows Erbs et al. (1982).

## 292 4 Results

### 293 4.1 Spectral and angular effect of clouds on PV performance

#### 294 4.1.1 Impact of cloud optical thickness

295 Figure 9a indicates that the in-band performance  $\rho^*$  decreases with optical thickness for all simulated SZAs. It  
 296 drops from 19.3 % to 15.8 % for  $\tau$  ranging from 0 to 50 when  $\text{SZA} = 70^\circ$ . This can be explained by the spectral  
 297 filtering of clouds that shifts the irradiance within the range  $[0 - \lambda_{\text{gap}}]$  towards the blue domain as the optical thickness  
 298 increases, combined with a reduced SR in this domain.

299 The opposite behaviour is generally observed for  $\text{SZA} < 50^\circ$  – domain over which most PV energy is harvested  
 300 – when the total POA irradiance is considered (Fig. 9b). Up to a critical optical thickness  $\tau_{\text{crit}}(\text{SZA})$ , clouds enhance

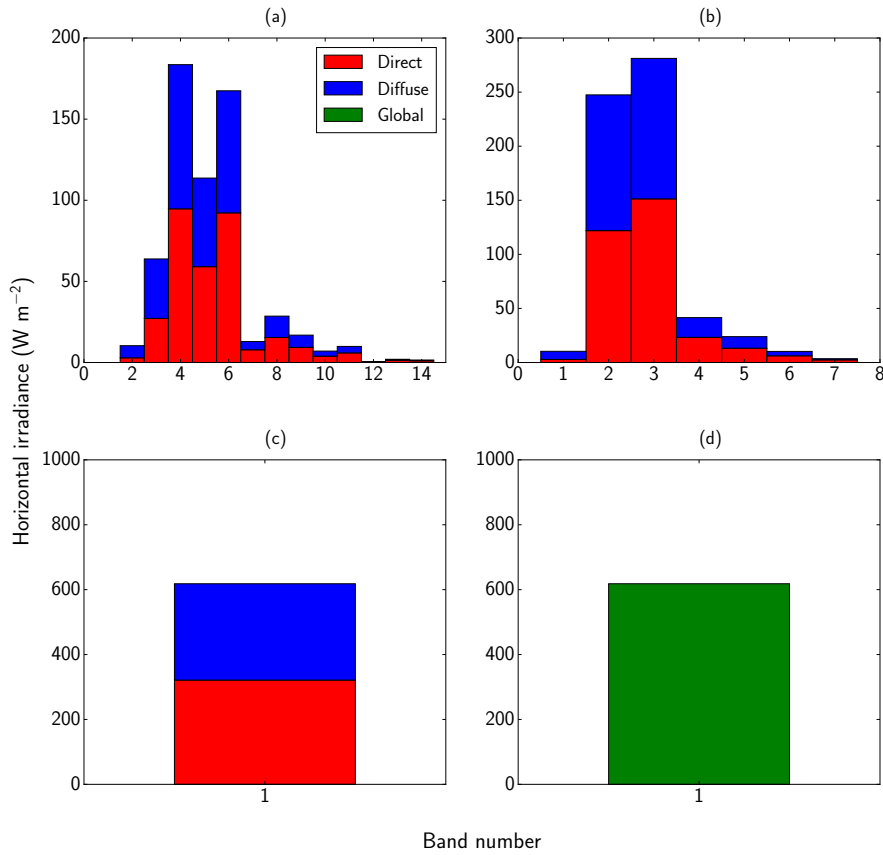


Figure 8: Illustration of the 4 input configurations obtained from ecRad simulations: 14 (a), 7 (b) and 1 (c) spectral bands, as well as solely GHI (d). The simulation corresponds to a cloudy atmosphere ( $\tau = 1.73$ ) with  $\text{SZA} = 48^\circ$ .

301 the PV performance  $\rho$ , with gains up to 5.7% (for  $\text{SZA} = 0^\circ$ ). The difference between  $\rho$  and  $\rho^*$  is interpreted as  
 302 follows : due to the spectral filtering of clouds, photons that are not energetic enough to be absorbed by the PV  
 303 module are filtered out by the clouds. The useful fraction (UF) of irradiance (hence  $\rho$ ) thus increases with  $\tau$ , as  
 304 illustrated for instance in Fig. 10. Likewise, the APE increases as the incident spectrum becomes richer in shorter  
 305 and more energetic wavelengths. For high optical thicknesses (above  $\tau_{\text{crit}}(\text{SZA})$ ),  $\rho$  starts to decrease. At such optical  
 306 thicknesses, wavelengths larger than  $\lambda_{\text{gap}}$  have been widely filtered out such that POA irradiance approaches useful  
 307 POA irradiance, and  $\rho$  behaves more like  $\rho^*$ . A distinct behaviour is observed for large SZAs. In such case, the cloud  
 308 effect is enhanced and direct radiation rapidly vanishes due to its long path through the cloud. The part of the spectrum  
 309 where the spectral response is maximum is thus quickly filtered out and  $\rho$  behaves as  $\rho^*$ . The conversion from  $\rho^*$  to  
 310  $\rho$  is equivalent to multiplying  $\rho^*$  by UF, which increases with  $\tau$  (Fig. 10), hence explaining the complex variations  
 311 observed in Fig. 9b, in particular for  $\tau < 5$ .

#### 312 4.1.2 Impact of the solar zenith angle

313 Figure 9b shows that under clear-sky conditions  $\rho$  increases with SZA, whilst the opposite prevails in cloudy  
 314 conditions. In addition, at SZA larger than  $\sim 50^\circ$ ,  $\rho$  does not increase monotonically with  $\tau$ . In clear-sky conditions,  
 315 direct radiation is the main contributor to the POA irradiance, and its contribution grows with SZA as it becomes more  
 316 and more normal to the module (Fig. 11b). For larger SZA, the contribution of direct radiation decreases because it be-  
 317 comes less perpendicular to the panel and because diffuse radiation increases with SZA. However,  $\rho$  further increases

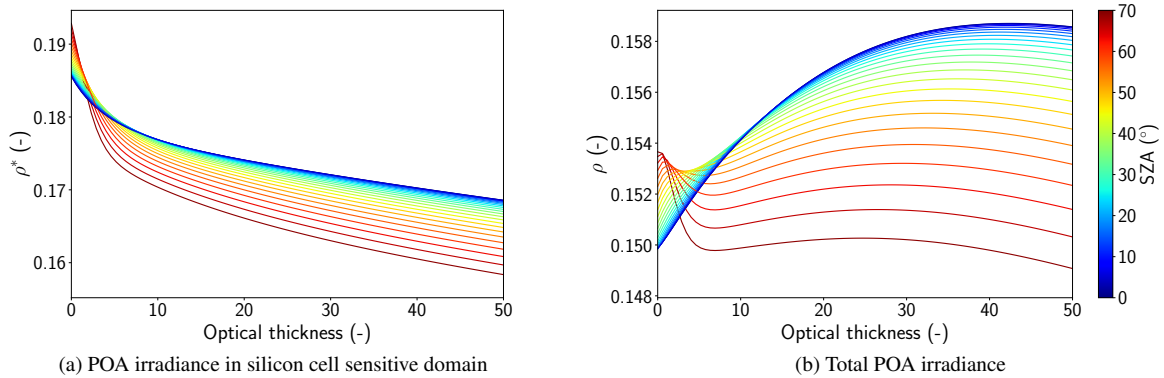


Figure 9: Simulated performance of the c-Si module as a function of cloud optical thickness and SZA.

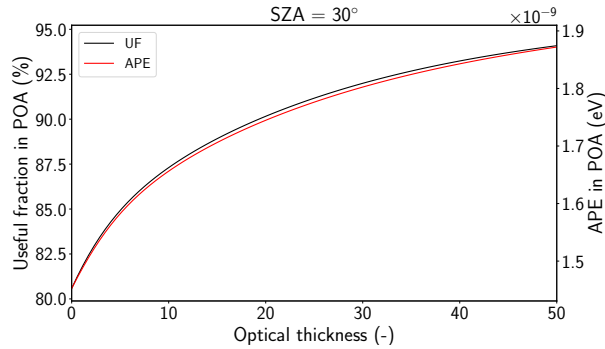


Figure 10: Variations of the useful fraction ( $\lambda < 1100$  nm) and average photon energy (over the whole spectrum) of POA irradiance with optical thickness for SZA =  $30^\circ$ .

318 because at the same time, the performance of the module increases due to the spectral changes of irradiance. Note that  
 319 this balance between relative contribution of direct radiation and spectral effects depends on the inclination angle of  
 320 the panel, so that slightly different dependences on SZA may be encountered at different  $\beta$ . On the contrary, for opti-  
 321 cally thick clouds, the POA irradiance is essentially diffuse and results from the mixing of direct and diffuse radiation  
 322 impacting the cloud top. The relative preponderance of blue light at cloud top increases with SZA, which explains  
 323 why the performance decreases with SZA. In other words, SZA has under clear skies a geometric effect through the  
 324 relative contribution of the more efficient direct irradiance, whereas under cloudy skies, SZA has a spectral effect on  
 325 PV performance similar to that of optical thickness due to the wavelength-selective Rayleigh scattering.

326  
 327 To conclude, the impact of clouds on radiation can be explained by two levels of spectral filtering. First, clouds  
 328 tend to increase the performance of a PV module as they filter out photons with insufficient energy. Second, due  
 329 to the shift from NIR towards the blue domain, the effect is opposite when only the useful irradiance is considered.  
 330 SZA also affects the performance, by controlling the contribution of direct radiation and the path length through the  
 331 atmosphere. This overall stresses that there is no simple relationship between POA irradiance and PV power.

#### 332 4.2 Spectral resolution

333 The previous section used 14-band irradiance inputs. Yet, irradiance obtained from measurements or atmospheric  
 334 models is often integrated over the whole SW domain or a limited number of bands. The following section investigates  
 335 the impact of this limited information on simulated power. PV power is simulated for all  $\{SZA, \tau\}$  combinations used

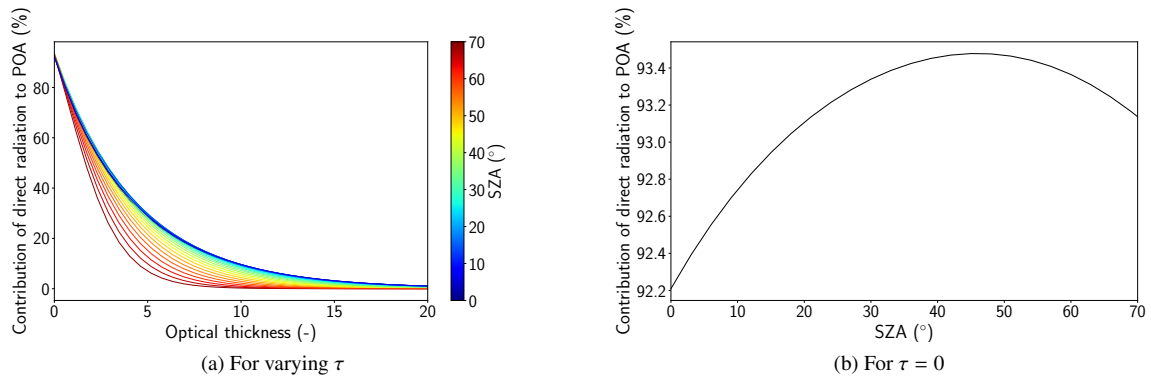


Figure 11: Contribution of the beam radiation to the total POA irradiance.

336 in Section 4.1, and the three degraded inputs introduced in Section 3.5. Figure 12 shows the relative difference between  
 337 the power simulated with the degraded inputs and the reference 14-band input.

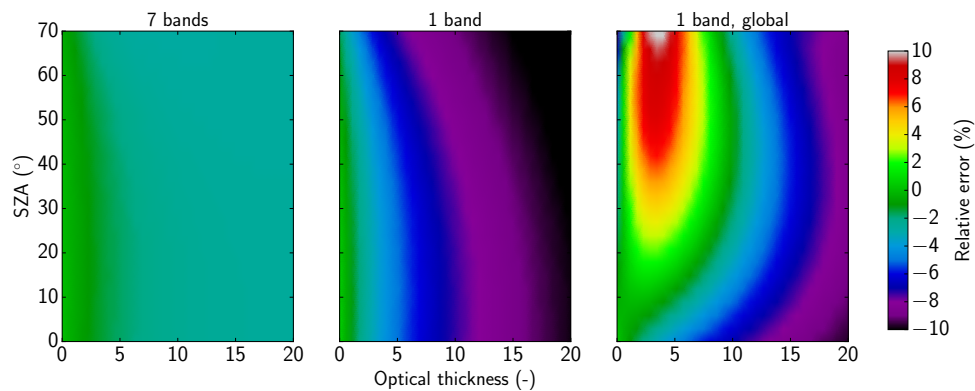


Figure 12: Relative error in simulated PV power as a function of  $\tau$  and SZA and for the 7-band, 1-band and 1-band global inputs, with respect to the 14-band input.

338 The 7-band configuration is more precise (up to -3% error) than the 1-band (up to -10% error). Generally, errors  
 339 increase with optical thickness, as spectral effects gain in importance. As the number of bands declines, spectral  
 340 filtering by clouds is less captured and cannot be correctly accounted for by the spectral refinement. The difference  
 341 between the 7- and 14-band configurations suggests that a dozen bands should practically be enough to achieve  
 342 satisfactory performance. Also, the reference ARTDECO spectra used for spectral refinement have been computed  
 343 under clear-sky conditions. Hence, when only one band is provided, the highly resolved irradiance corresponds to a  
 344 clear-sky spectrum, thus leading to underestimated power, which explains the negative errors. The sensitivity to SZA  
 345 remains limited thanks to the use of SZA-interpolated ARTDECO reference spectra. When only the GHI is known,  
 346 the relative errors range from -10 % to 10 % and present no general trend over SZA or  $\tau$ . This largest range of relative  
 347 errors and the non-monotonous variability with atmospheric conditions point out that the GHI is not a sufficient input  
 348 parameter for PV modelling. Despite this deficiency, it probably remains the most extensively used quantity to feed  
 349 PV models.

350 Although Fig. 12 was obtained with an ideal spectral response, it was also computed (not shown) assuming  
 351 a more realistic spectral response for the c-Si module (from [https://pvpmc.sandia.gov/modeling-steps/  
 352 2-dc-module-iv/effective-irradiance/spectral-response/](https://pvpmc.sandia.gov/modeling-steps/2-dc-module-iv/effective-irradiance/spectral-response/)). The obtained patterns are very similar, but the relative errors are approximately 50% larger, highlighting that the spectral effect might be even more significant  
 353 with a realistic spectral response. Likewise, all the results presented above have been obtained without aerosols.  
 354



355 Quantitative results may slightly change in the presence of aerosols but the overall trends and general conclusions  
356 would remain the same.

## 357 5 Discussion

### 358 5.1 Comparison to observations

#### 359 5.1.1 Previous experimental studies

360 In the case of c-Si cells under clear skies, Stark and Theristis (2015) found that increasing SZAs causes spectral  
361 gains up to  $SZA \approx 75 - 80^\circ$  and losses beyond. Our results for  $SZA < 70^\circ$  support these results. Likewise the  
362 observations reported by Nofuentes et al. (2014) confirm the positive effect of clouds on  $\rho$ . The variations of  $\pm 5\%$   
363 they noticed compared to STC are slightly larger than those obtained in this paper. Yet, their results are based on  
364 observations, meaning that other atmospheric variables may amplify the spectral effects. Last, Jardine et al. (2001)  
365 conclude that c-Si cells work more efficiently under clear skies based on a measurement campaign and an estimation  
366 of the cloud cover. However, Jardine et al. (2001) lack details on how PV efficiency is computed and their approach  
367 based on the cloud cover  $K_t$  instead of the cloud optical thickness does not enable a clear comparison between their  
368 results and this study.

#### 369 5.1.2 In situ observations at SIRTA

370 Here an attempt is made to compare the PV performance obtained in the numerical simulations to observations  
371 made at SIRTA. To this end, the measured performance  $\rho$  is compared to that simulated in Fig. 9b. A  $SZA$  of  
372  $30^\circ$  is chosen because it corresponds to summer conditions at noon at SIRTA and because Fig. 9b suggests that  $\rho$   
373 is more sensitive to  $\tau$  at low  $SZA$ . To be consistent with the simulations, the measured power is first corrected to  
374 the equivalent power at  $25^\circ\text{C}$  ( $T_{c,STC}$ ). Then, one performance value per day satisfying the following conditions  
375 is retained: i) only measurements taken between 11h50 and 12h10 and such that  $SZA$  is between  $27$  and  $33^\circ$  are  
376 used and averaged in order to be comparable with the theoretical results obtained for  $SZA = 30^\circ$ ; ii) at least two  
377 such measurements are available; iii) the difference between the maximum and minimum incident SW radiation  
378 measurements is less than 0.3 times the average value to ensure relative stability of the cloud cover. The optical  
379 thickness  $\tau$  of *in situ* clouds was estimated from the measured atmospheric transmittance, following eq. (9) of Barnard  
380 and Long (2004)<sup>7</sup>. Fig. 13 shows the measured and simulated performances as a function of cloud optical thickness. It  
381 indicates that the observations globally agree with the simulations in terms of absolute values (relative differences less  
382 than 7%). Significant deviations nevertheless remain and the dependence of  $\rho$  on  $\tau$  is not obvious in the observations,  
383 making this comparison somehow inconclusive. This is not completely surprising because the simulations consider a  
384 fixed atmosphere with horizontally uniform cloud properties, whereas observations correspond to varying atmospheric  
385 conditions where physical quantities such as cloud geometry, cloud fraction, humidity and aerosol optical depth affect  
386 the spectral and angular properties of the irradiance, probably competing with clouds. Also, the optical thickness  
387 of a heterogeneous cloud is hard to define, which is further biased by the distance between the instruments related  
388 to irradiance and the PV modules. This suggests that assessing the impact of clouds on PV performance based on  
389 measurements is challenging because the uncertainty of measurements is similar in magnitude to the expected impact  
390 of clouds. Although a more quantitative identification of the sources of error for PV performance simulations would  
391 definitely be useful to improve PV models, this would require a more extensive set of measurements and a more  
392 thorough data analysis than intended in this study.

### 393 5.2 Application to NWP outputs

394 The present study is intentionally academic and does not pretend to quantify the global impact of using refined  
395 NWP outputs for PV power forecast or to demonstrate the quantitative benefit of using the developed PV model. Such  
396 an integrated investigation is beyond the scope of the present paper. It would deserve a distinct dedicated work

---

<sup>7</sup>  $\tau = \exp(2.15 + \alpha_s + 1.91 \arctanh(1 - 1.74r))$ , where the surface albedo  $\alpha_s = 0.2$  and  $r = \frac{\text{GHI}}{\text{GHI}_{cs}\mu_0^{1/4}}$ .  $\text{GHI}_{cs}$  is the theoretical GHI in clear sky conditions computed with ARTDECO, and  $\mu_0 = \cos(SZA)$ .

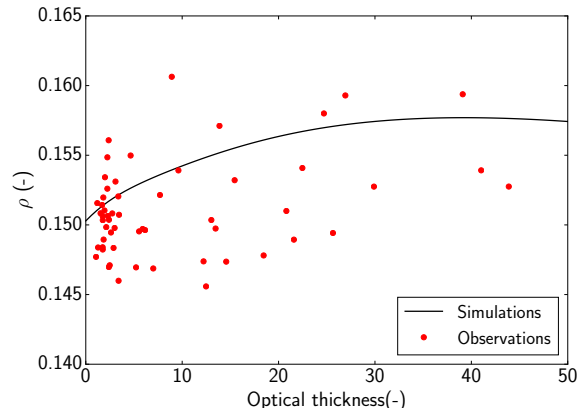


Figure 13: Measured and simulated performances as a function of cloud optical thickness for  $SZA = (30 \pm 3)^\circ$  and Sun-facing PV module. The measured performance is corrected to represent the equivalent performance at  $T_{c,STC}$ .

400 along with additional field observations. However, because the findings of Section 4.2 were obtained in very idealistic  
 401 atmospheric conditions, this section aims at exploring more realistic and diverse atmospheric configurations. To this  
 402 end, simulations are performed with the research atmospheric model Meso-NH (Lac et al., 2018) on a domain of  $80$   
 403  $\times 80$  km centered on the SIRTAs. Each simulation lasts 24 hours and can be considered as a weather forecast. The  
 404 following analysis focuses on June 2017. A month-long simulation enables to cover various atmospheric simulations  
 405 as intended. June was chosen because it is when cumulated PV production is generally the largest. Atmospheric  
 406 reanalysis from the AROME operational model (Seity et al., 2011) are used to initialize the Meso-NH simulations  
 407 and to provide boundary conditions. The solar irradiance in Meso-NH is computed with ecRad, and the model was  
 408 updated to output the direct and diffuse spectral irradiances in 14 spectral bands at the SIRTAs. As in Section 4.2,  
 409 these irradiances were post-processed to obtain various configurations which were fed into the PV model, allowing  
 410 to compare the time series of PV power. Clouds in the simulations can be multi-layer and have physical properties  
 411 varying with altitude, including effective radius which is diagnosed after eq. (24)<sup>8</sup> of Martin et al. (1994), thus covering  
 412 a variety of cloud conditions. In addition, aerosols optical depths are prescribed in Meso-NH based on climatological  
 413 values.

414 The mean relative error in simulated PV power over June 2017 is 0.36 % with 7 bands, and 1.00 % for 1 band.  
 415 When only GHI is used, the production is underestimated by only 0.30 % but this is the result of error compensation at  
 416 different SZA. The mean absolute relative error for this configuration is actually 2.78 %. Because spectral effects are  
 417 known to depend on PV technology, similar computations were performed for a CdTe panel which is more wavelength-  
 418 selective ( $\lambda_{gap} = 806$  nm). This resulted in larger mean relative errors of -0.5, 2.1 and 5.0 % for the three configurations  
 419 detailed above.

420 Figure 14 shows the relative difference of simulated PV power between the degraded configurations and the refer-  
 421 ence 14-band configuration. The densest regions of points correspond to clear-sky conditions, which were prevailing  
 422 in June 2017. In such conditions, the impact of degrading resolution is very marginal for the 7 bands and 1 band con-  
 423 figurations, but it becomes significant for the 1 band global configuration as SZA increases, that is when the reference  
 424 power decreases. The impact of clouds is in most cases to reduce the estimated PV power. This underestimation is  
 425 around 2% for the 7 band configuration, but it often exceeds 10 % for the 1 band configurations and reaches 20% for  
 426 the 1 band global configuration. These results are consistent with those shown in Fig. 12, but encompass much more  
 427 realistic cloudy conditions than those investigated in Section 4.2.

428 The Meso-NH simulations confirm that in cloudy conditions a poor representation of the spectral distribution of  
 solar irradiance can result in large errors of PV power and consequently highlight the need for detailed irradiance  
 inputs in cloudy conditions, which is the primary objective of the study. The monetary impact of the identified errors  
 is very hard to estimate. It would require large scale NWP simulations over long periods, and a proper treatment of

<sup>8</sup>with  $N_{tot} = 900 \text{ cm}^{-3}$  and  $d = 0.43$ .

429 the penalties resulting from unbalance between day-ahead energy forecast and actual production (Antonanzas et al.,  
 430 2017). Likewise, the impact on the management of the electricity grid will be very location-dependent and cannot be  
 431 assessed based on this work. The operational impact of the present findings and the complementary analysis needed  
 432 to tackle the pointed issues are thus left to experts.

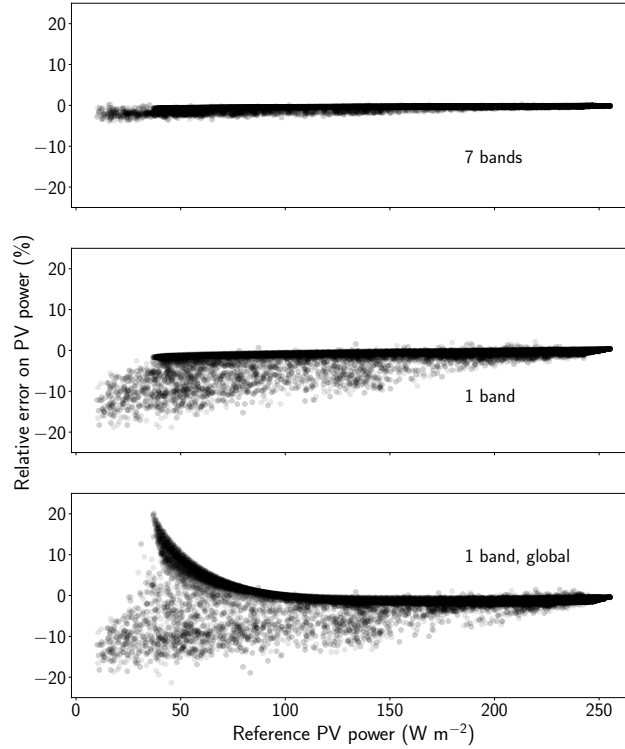


Figure 14: Relative difference in PV power for various configurations of solar irradiance inputs with respect to the reference 14-band configuration, as a function of the reference power. The reference solar irradiance corresponds to 1-min-resolution Meso-NH simulations at SIRTa for June 2017. Other configurations are obtained via degradation of the reference configuration. Only simulations for  $\text{SZA} < 70^\circ$  and  $\text{PV}_{\text{ref}} > 10 \text{ W m}^{-2}$  are used.

### 433 5.3 Practical impacts

434 This study shows that clouds alter PV power not only because they reduce the available POA irradiance, but also  
 435 because they alter the performance of PV cells through spectral filtering. This is critical for studies using climate  
 436 models to investigate the effect of climate change on PV performance or to compute PV potential atlases.

437 Our results clearly indicate that a given POA irradiance can result in different PV power because the relationship  
 438 depends on atmospheric conditions. More importantly, GHI is shown to be far from sufficient to accurately model  
 439 PV power as it lacks both angular and spectral information. Though most PV models make a hypothesis on the  
 440 repartition between direct and diffuse radiation, only a few attempt to correct PV performance for the corresponding  
 441 spectral changes. In both cases, GHI is used to deduce the direct and diffuse irradiances thanks to measured or  
 442 simulated ancillary quantities, which means that PV models attempt to reconstruct atmospheric conditions. The aim  
 443 of the newly developed PV model is to overcome this loss of information between the atmospheric model and the PV  
 444 model by directly exploiting the internal variables of atmospheric models. As such it is expected to reduce the overall  
 445 computation time by limiting the number of extra steps. Hence the apparent complexity of the physical model should  
 446 not be a critical obstacle to its utilization, unless it is proven definitely too complex for specific applications.

447 The present work focused on c-Si cells, which are less sensitive to spectral effects than other solar cells with a  
 448 smaller  $\lambda_{\text{gap}}$  (Nofuentes et al., 2014; Dirnberger et al., 2015) such as CdTe and a-Si cells, as illustrated in Section 5.2.

449 The impact of clouds on PV performance are time, location and technology dependent, so that a more quantitative  
450 analysis would require a dedicated study that is beyond the scope of the present paper. For instance, the impacts are  
451 expected to be more significant in cloudy areas, while they may be insignificant in sunny areas. However, accounting  
452 for spectral effects would be all the more relevant for such sensitive technologies and could be the focus of future  
453 studies.

## 454 **6 Conclusion**

455 This study investigated the benefit of using angularly and spectrally detailed irradiance inputs in PV models that  
456 convert atmospheric variables into PV power. Such a model has been developed with the intent to fully take advantage  
457 of the internal spectral radiative quantities of atmospheric models or radiative transfer codes. It properly accounts for  
458 the spectral and angular impacts of incident radiation on PV performance, in particular through the spectral resolution  
459 refinement of the irradiance inputs which is essential to cope with the low spectral resolution of atmospheric models  
460 outputs and to match the sharp spectral response of PV cells. Based on this model, the sensitivity of simulated PV  
461 power to the resolution of the irradiance inputs has been explored. This work indicates that the presence of clouds,  
462 through spectral filtering, can increase PV performance by more than 5%, and that similar variations are expected  
463 when varying the solar zenith angle (SZA). The model was also used to assess the errors committed when incident  
464 irradiance input to the PV model is only poorly known, that is when it lacks spectral or angular information. It was  
465 shown that using a single spectral band results in errors up to 10 %, which amount to 15 % when solely the Global  
466 Horizontal Irradiance (GHI) is fed into the PV model. It also suggests that a dozen spectral bands should be sufficient  
467 to correctly account for the spectral effects of clouds. These theoretical findings were supported by the analysis  
468 of spectral irradiances outputs of a NWP model corresponding to complex and more realistic atmospheric states.  
469 Although most PV models use standard atmospheric inputs which lack information, this study highlights that efforts  
470 should be made to fully take advantage of atmospheric models which generally deal with more informative internal  
471 variables, stressing the need for closer ties between the solar energy and atmospheric sciences communities. This is all  
472 the more relevant as this information could be gained without any increase in computation efficiency. Practically, these  
473 internal variables are not stored nowadays, simply because the extra storage space it would imply is not justified by  
474 well identified applications. The solar energy community could make it change by showing a strong interest for such  
475 quantities. Even though the highlighted spectral effects are much smaller than the errors in irradiance forecasts due  
476 to the inherent complexity of treating cloud heterogeneity and 3D radiative effects in NWP models, properly handling  
477 the currently available products can already substantially help to refine solar power prediction reliability. This project  
478 paves the way to further analyses related to the impact of spectral and angular properties of radiation on PV power. In  
479 particular, a similar study on aerosols shall be performed in the future, because alike clouds, different aerosols have  
480 different spectral and angular impacts on solar radiation, which cannot be quantified solely by their optical depth.

## 481 **Acknowledgements**

482 This work was supported by the French national program LEFE/INSU through the CASPER project and the  
483 TREND-X research program of Ecole Polytechnique. The authors are grateful to Laurent Labonnote for helpful  
484 discussions on ARTDECO and to Christine Lac for the design of Meso-NH simulations.

## 485 **References**

- 486 Antonanzas, J., Osorio, N., Escobar, R., Urraca, R., Martinez-de Pison, F., Antonanzas-Torres, F., 2016. Review of photovoltaic power forecasting.  
487 *Solar Energy* 136, 78–111.
- 488 Antonanzas, J., Pozo-Vázquez, D., Fernandez-Jimenez, L., Martinez-de Pison, F., 2017. The value of day-ahead forecasting for photovoltaics in  
489 the Spanish electricity market. *Solar Energy* 158, 140–146.
- 490 Badescu, V., 2002. 3D isotropic approximation for solar diffuse irradiance on tilted surfaces. *Renewable Energy* 26 (2), 221–233.
- 491 Badosa, J., Bourdin, V., Haefelin, M., Le, G., 2015. Multi-technology photovoltaic module test bench on the SIRTAs meteorological and climate  
492 observatory. In: 31st European PV Solar Energy Conference and Exhibition.
- 493 Barnard, J. C., Long, C. N., 2004. A simple empirical equation to calculate cloud optical thickness using shortwave broadband measurements.  
494 *Journal of Applied Meteorology* 43 (7), 1057–1066.
- 495 Brandemuehl, M., Beckman, W., 1980. Transmission of diffuse radiation through CPC and flat plate collector glazings. *Solar Energy* 24 (5),  
496 511–513.

497 Da Rosa, A. V., 2005. Fundamentals of renewable energy processes, 1st Edition. Academic Press.

498 Das, U. K., Tey, K. S., Seyedmahmoudian, M., Mekhilef, S., Idris, M. Y. I., Van Deventer, W., Horan, B., Stojcevski, A., 2018. Forecasting of  
499 photovoltaic power generation and model optimization: A review. *Renewable and Sustainable Energy Reviews* 81, 912–928.

500 De Soto, W., Klein, S., Beckman, W., 2006. Improvement and validation of a model for photovoltaic array performance. *Solar Energy* 80 (1),  
501 78–88.

502 Diagne, M., David, M., Lauret, P., Boland, J., Schmutz, N., 2013. Review of solar irradiance forecasting methods and a proposition for small-scale  
503 insular grids. *Renewable and Sustainable Energy Reviews* 27, 65–76.

504 Dimberger, D., Blackburn, G., Müller, B., Reise, C., 2015. On the impact of solar spectral irradiance on the yield of different PV technologies.  
505 *Solar Energy Materials and Solar Cells* 132, 431–442.

506 Duffie, J. A., Beckman, W. A., 2013. *Solar engineering of thermal processes*. John Wiley & Sons.

507 Edwards, J., Slingo, A., 1996. Studies with a flexible new radiation code. I: Choosing a configuration for a large-scale model. *Quarterly Journal of*  
508 *the Royal Meteorological Society* 122 (531), 689–719.

509 Erbs, D., Klein, S., Duffie, J., 1982. Estimation of the diffuse radiation fraction for hourly, daily and monthly-average global radiation. *Solar Energy*  
510 28 (4), 293–302.

511 Frouin, R., Ramon, D., Jolivet, D., Compiègne, M., 2018. Specifying algorithm uncertainties in satellite-derived PAR products. In: *Remote Sensing*  
512 *of the Open and Coastal Ocean and Inland Waters*. Vol. 10778. International Society for Optics and Photonics, p. 107780W.

513 Ghitas, A. E., 2012. Studying the effect of spectral variations intensity of the incident solar radiation on the Si solar cells performance. *NRIAG*  
514 *Journal of Astronomy and Geophysics* 1 (2), 165–171.

515 Gottschalg, R., Betts, T., Williams, S., Sauter, D., Infield, D., Kearney, M., 2004. A critical appraisal of the factors affecting energy production  
516 from amorphous silicon photovoltaic arrays in a maritime climate. *Solar Energy* 77 (6), 909–916.

517 Gottschalg, R., Infield, D., Kearney, M., 2003. Experimental study of variations of the solar spectrum of relevance to thin film solar cells. *Solar*  
518 *Energy materials and solar cells* 79 (4), 527–537.

519 Green, M. A., 1982. Accuracy of analytical expressions for solar cell fill factors. *Solar Cells* 7 (3), 337–340.

520 Gueymard, C. A., Ruiz-Arias, J. A., 2016. Extensive worldwide validation and climate sensitivity analysis of direct irradiance predictions from  
521 1-min global irradiance. *Solar Energy* 128, 1–30.

522 Haeffelin, M., Barthès, L., Bock, O., Boitel, C., Bony, S., Bouniol, D., Chepfer, H., Chiriaco, M., Cuesta, J., Delanoë, J., et al., 2005. SIRTa, a  
523 ground-based atmospheric observatory for cloud and aerosol research. In: *Annales Geophysicae*. Vol. 23. pp. 253–275.

524 Hale, G. M., Querry, M. R., 1973. Optical constants of water in the 200-nm to 200- $\mu\text{m}$  wavelength region. *Applied Optics* 12 (3), 555–563.

525 Hess, M., Koepke, P., Schult, I., 1998. Optical properties of aerosols and clouds: The software package OPAC. *Bulletin of the American meteorolo-*  
526 *gical society* 79 (5), 831–844.

527 Hogan, R. J., Bozzo, A., 2018. A flexible and efficient radiation scheme for the ECMWF model. *Journal of Advances in Modeling Earth Systems*.

528 Jardine, C. N., Conibeer, G. J., Lane, K., 2001. PV-COMPARE: direct comparison of eleven PV technologies at two locations in northern and  
529 southern Europe. In: *Seventeenth EU PVSEC*.

530 Jerez, S., Tobin, I., Vautard, R., Montávez, J. P., López-Romero, J. M., Thais, F., Bartok, B., Christensen, O. B., Colette, A., Déqué, M., et al.,  
531 2015. The impact of climate change on photovoltaic power generation in Europe. *Nature communications* 6, 10014.

532 Jimenez, P. A., Hacker, J. P., Dudhia, J., Haupt, S. E., Ruiz-Arias, J. A., Gueymard, C. A., Thompson, G., Eidhammer, T., Deng, A., 2016. WRF-  
533 Solar: Description and clear-sky assessment of an augmented NWP model for solar power prediction. *Bulletin of the American Meteorological*  
534 *Society* 97 (7), 1249–1264.

535 Joseph, J. H., Wiscombe, W., Weinman, J., 1976. The delta-Eddington approximation for radiative flux transfer. *Journal of the Atmospheric*  
536 *Sciences* 33 (12), 2452–2459.

537 King, D. L., Boyson, W. E., Kratochvil, J. A., 2004. Photovoltaic array performance model. Tech. rep., Sandia National Laboratories.

538 King, D. L., Kratochvil, J. A., Boyson, W. E., 1997. Measuring solar spectral and angle-of-incidence effects on photovoltaic modules and solar  
539 irradiance sensors. In: *Photovoltaic Specialists Conference, 1997.*, Conference Record of the Twenty-Sixth IEEE. IEEE, pp. 1113–1116.

540 Kim, B., Topic, M., 2017. Diffuse and direct light solar spectra modeling in PV module performance rating. *Solar Energy* 150, 310–316.

541 Kokhanovsky, A., 2004. Optical properties of terrestrial clouds. *Earth-Science Reviews* 64 (3-4), 189–241.

542 Kostylev, V., Pavlovski, A. e. a., 2011. Solar power forecasting performance-towards industry standards. In: *1st International Workshop on the*  
543 *Integration of Solar Power into Power Systems*, Aarhus, Denmark.

544 Lac, C., Chaboureaud, P., Masson, V., Pinty, P., Tulet, P., Escobar, J., Leriche, M., Barthe, C., Aouizerats, B., Augros, C., et al., 2018. Overview of  
545 the Meso-NH model version 5.4 and its applications. *Geoscientific Model Development* 11, 1929–1969.

546 Liou, K.-N., 2002. *An introduction to atmospheric radiation*. Vol. 84. Academic press.

547 Lohou, F., Patton, E. G., 2014. Surface energy balance and buoyancy response to shallow cumulus shading. *Journal of the Atmospheric Sciences*  
548 71 (2), 665–682.

549 Lorenzo, E., 2003. Energy collected and delivered by PV modules. *Handbook of photovoltaic science and engineering*, 905–970.

550 Marion, B., 2012. Influence of atmospheric variations on photovoltaic performance and modeling their effects for days with clear skies. In: *2012*  
551 *38th IEEE Photovoltaic Specialists Conference*. IEEE, pp. 003402–003407.

552 Martin, G., Johnson, D., Spice, A., 1994. The measurement and parameterization of effective radius of droplets in warm stratocumulus clouds.  
553 *Journal of the Atmospheric Sciences* 51 (13), 1823–1842.

554 Mayer, B., Kylling, A., 2005. The libRadtran software package for radiative transfer calculations-description and examples of use. *Atmospheric*  
555 *Chemistry and Physics* 5 (7), 1855–1877.

556 Messenger, R. A., Abtahi, A., 2017. *Photovoltaic systems engineering*. CRC press.

557 Mittag, M., Vogt, L., Herzog, C., Pfreundt, A., Shahid, J., Neuhaus, D. H., Wirth, H., 2019. Thermal Modelling of Photovoltaic Modules in  
558 Operation and Production. In: *36th European Photovoltaic Solar Energy Conference and Exhibition (EUPVSEC)*.

559 Mlawer, E. J., Taubman, S. J., Brown, P. D., Iacono, M. J., Clough, S. A., 1997. Radiative transfer for inhomogeneous atmospheres: RRTM, a  
560 validated correlated-k model for the longwave. *Journal of Geophysical Research: Atmospheres* 102 (D14), 16663–16682.

561 Morcrette, J., Barker, H., Cole, J., Iacono, M., Pincus, R., 2008. Impact of a new radiation package, McRad, in the ECMWF Integrated Forecasting

562 System. Monthly weather review 136 (12), 4773–4798.

563 Myers, D., Emery, K., Gueymard, C., 2002. Proposed reference spectral irradiance standards to improve concentrating photovoltaic system design  
564 and performance evaluation. In: Photovoltaic Specialists Conference, 2002. Conference Record of the Twenty-Ninth IEEE. IEEE, pp. 923–926.

565 Myers, D. R., Gueymard, C. A., 2004. Description and availability of the SMARTS spectral model for photovoltaic applications. In: SPIE proceed-  
566 ings series. Society of Photo-Optical Instrumentation Engineers, pp. 56–67.

567 Nielsen, K. P., Gleeson, E., Rontu, L., 2014. Radiation sensitivity tests of the HARMONIE 37h1 NWP model. Geoscientific Model Development  
568 7 (4), 1433–1449.

569 Nofuentes, G., García-Domingo, B., Muñoz, J., Chenlo, F., 2014. Analysis of the dependence of the spectral factor of some PV technologies on the  
570 solar spectrum distribution. Applied Energy 113, 302–309.

571 Nofuentes, G., Gueymard, C., Aguilera, J., Pérez-Godoy, M., Charte, F., 2017. Is the average photon energy a unique characteristic of the spectral  
572 distribution of global irradiance? Solar Energy 149, 32–43.

573 Norton, M., Amillo, A. G., Galleano, R., 2015. Comparison of solar spectral irradiance measurements using the average photon energy parameter.  
574 Solar Energy 120, 337–344.

575 Oreopoulos, L., Mlawer, E., Delamere, J., Shippert, T., Cole, J., Fomin, B., Iacono, M., Jin, Z., Li, J., Manners, J., et al., 2012. The continual  
576 intercomparison of radiation codes: Results from phase I. Journal of Geophysical Research: Atmospheres 117 (D6).

577 Perez, R., Ineichen, P., Seals, R., Michalsky, J., Stewart, R., 1990. Modeling daylight availability and irradiance components from direct and global  
578 irradiance. Solar Energy 44 (5), 271–289.

579 Seity, Y., Brousseau, P., Malardel, S., Hello, G., Bénard, P., Bouttier, F., Lac, C., Masson, V., 2011. The AROME-France convective-scale opera-  
580 tional model. Monthly Weather Review 139 (3), 976–991.

581 Singh, P., Ravindra, N. M., 2012. Temperature dependence of solar cell performance – an analysis. Solar Energy Materials and Solar Cells 101,  
582 36–45.

583 Sjerps-Koomen, E., Alsema, E., Turkenburg, W., 1996. A simple model for PV module reflection losses under field conditions. Solar Energy 57 (6),  
584 421–432.

585 Skoplaki, E., Boudouvis, A., Palyvos, J., 2008. A simple correlation for the operating temperature of photovoltaic modules of arbitrary mounting.  
586 Solar Energy Materials and Solar Cells 92 (11), 1393–1402.

587 Stamnes, K., Tsay, S.-C., Wiscombe, W., Jayaweera, K., 1988. Numerically stable algorithm for discrete-ordinate-method radiative transfer in  
588 multiple scattering and emitting layered media. Applied optics 27 (12), 2502–2509.

589 Stark, C., Theristis, M., 2015. The impact of atmospheric parameters on the spectral performance of multiple photovoltaic technologies. In:  
590 Photovoltaic Specialist Conference (PVSC), 2015 IEEE 42nd. IEEE, pp. 1–5.